ACDIS
Research
Report

Global Heat Balance Equation Probability Distributions and Extrapolations

Chenghao Ding
Department of Nuclear, Plasma, and Radiological Engineering
University of Illinois at Urbana-Champaign

Clifford E. Singer
Program in Arms Control & Domestic and International Security
University of Illinois at Urbana-Champaign

Research of the Program in Arms Control
& Domestic and International Security

University of Illinois at Urbana–Champaign

July 2022

The research for this publication is supported by the University of Illinois. It is produced by the Program in Arms Control & Domestic and International Security at the University of Illinois at Urbana-Champaign.

ACDIS Publication Series: The ACDIS *Occasional Paper* series is designed for circulating the scholarly analytical results of faculty, students, and visiting researchers associated with ACDIS. The ACDIS *Research Reports* series publishes technical reports and findings from security related research. The ACDIS *Commentary* series serves to inform U.S. and international policy decisions. The ACDIS *International Security Policy Brief* series contains previous works with a purpose similar to those in the *Commentary* series. ACDIS *Swords and Ploughshares* contains archives of a periodic journal of collected articles aimed at a general audience. For additional information and to download publications, visit the ACDIS home page at: http://acdis.illinois.edu/

Published 2022 by ACDIS//ACDIS DIN:6.2022

University of Illinois at Urbana–Champaign 359 Armory Building, 505 E. Armory Ave.
Champaign, IL 61820-6237

Series Editor: Jazmin Tejeda

Global Heat Balance Equation Probability Distributions and Extrapolations

CHENGHAO DING
Department of Nuclear, Plasma, and Radiological Engineering
University of Illinois at Urbana Champaign

CLIFFORD E. SINGER
csinger@illinois.edu
Program in Arms Control & Domestic and International Security
University of Illinois at Urbana Champaign

Probability distributions for extrapolated global average temperature with different atmospheric carbon emissions options are based on data-calibrated probability distributions for four parameters affecting solutions of a global heat balance equation. These parameters control climate sensitivity, thermal inertia, efficacy of radiative forcing from tropospheric aerosols, and the difference between thermometer measurements and the temperature in equilibrium with an earlier radiative forcing approximated as having been constant. Inputs used for data calibration are annually averaged global average temperature and rates of change of earth's stored energy driven by an imbalance between radiative forcing and losses. Principal component analysis allows derivation of a quadrivalent normal distribution that provides useful approximations to the probability of the observations as a function of the four uncertain parameters. Random samples of the probability distributions are used to define and plot cumulative probability distributions for the response of extrapolated global average temperature to different anthropogenic atmospheric carbon emissions futures.

1. Background

This is the sixth in a series of reports describing components of a revision an earlier form [1] of the Climate Action Gaming Experiment (CAGE). The five previous reports in this series developed the inputs for the extrapolations described here. The titles of those reports are [2]

CAGER1: Climate Action Game Experiment Motivation and Role of Radiative Forcing
CAGER2: Calibration and Extrapolation of a Simple Global Carbon Balance Model
CAGER3: Non-anthropogenic Influences on Global Average Temperature
CAGER4: Globoal Heat Balance Model Parameter Calibration
CAGER5: Extrapolations of Global Average Temperature, Sea Level Rise, and Ocean pH Change

CAGER1 gives equations and parameters for fits to historical data needed for most of the contributions to radiative forcing used here. CAGER2 gives equations and parameters for a set of extrapolations of atmospheric concentrations $< CO_2 >$ of carbon dioxide. CAGER3 gives parameters for extrapolation of solar radiative forcing after removal of c. 11 year Schwabe cycle variations. It also provides corrections, used here, to global average temperature input data to account for transient effects correlated with the El Niño Southern Oscillation (ENSO), with Schwabe cycle solar irradiance variations, and with stratospheric aerosols from large volcanic eruptions. CAGER4 gives probability maximizing parameters needed for extrapolation of global average temperature by solving the global heat balance equation

$$c_{th}\tau' = F_{na} + c_a F_a - \tau/\beta \tag{1.1}$$

Here F_a is a nominal estimate of (negative) radiative forcing from tropospheric aerosols [3], and F_{na} sums all other radiative forcing, except for from Schwabe cycle solar irradiance variations and effects of large volcanic eruptions discussed in CAGER3. The parameter c_a is referred to here as the tropospheric aerosol efficacy. This equation can be solved after replacing the thermal inertia parameter by the thermal equilibration rate $\mu = 1/(\beta c_{th})$. The parameter β, with units of $°C/(W/m^2)$, is referred to here as the climate sensitivity. This parameter is not to be confused with what is commonly called the equilibrium climate sensitivity and has units of °C [3]. CAGER5 presents

deterministic outcomes for implementation of five future global anthropogenic atmospheric carbon emissions policies. The present report presents probability distributions for those extrapolated temperatures at future dates.

CAGER4 contains an expression for the probability $P(\beta, \mu, c_a, \tau_0, c_s, c_v, c_e, \sigma_\tau, \sigma_{E_*}, \sigma_{out})$ of obtaining a set of 74 annually and globally geographically averaged temperature estimates and 27 estimates of the rate of change of global stored energy driven by global radiative imbalance, as described below in Appendix A. Of the ten arguments of this function, only the first three are needed for extrapolating global average temperature for a given evolutions of the radiative forcing functions F_{na} and F_a. Not being needed for temperature extrapolations, the last three arguments are treated as nuisance parameters and integrated over. Also not needed for temperature extrapolations in the absence of large volcanic eruptions and averaged over Schwabe solar cycle and ENSO oscillations are the temperature transient amplitude parameters $\{c_s,\ c_v,\ c_e\}$. These could be integrated over, but a simpler approach that gives very similar temperature extrapolations is to fix them at their values by maximizing the probability function integrated over $\{\sigma_\tau, \sigma_{E_*}, \sigma_{out}\}$. Doing so gives a function of four variables that can be approximated by a function of the form

$$P_4(\beta, \mu, c_a, \tau_0) = ((2\pi)^2 \sigma_1 \sigma_2 \sigma_3 \sigma_4)^{-2} e^{-(1/2)\sum_{i=1}^{4} (v_i/\sigma_i)^2} \tag{1.2}$$

where v_i are linear functions of $\{\beta, \mu, c_a, \tau_0\}$. Denoting the parameters $\{\beta, \mu, c_a, \tau_0\}$ as respective values of x_j for $j = 1 \ldots 4$ and their overall probability maximizing values as $\hat{x}_j$, the linear relationship between v_i and $\{\beta, \mu, c_a, \tau_0\}$ is

$$v_i = \sum_{j=1}^{4} e_{ij}(x_j - \hat{x}_j)/\hat{x}_j \tag{1.3}$$

where the values of e_{ij} are listed in Table 1. Also listed in Table 1 are the values of the probability maximizing parameters and of the scale parameters σ_i in equation 1.2. Random samples of these parameters are found by picking random samples of the v_i and then inverting equations (1.3) to find $\{\beta, \mu, c_a, \tau_0\}$.

Table 1. Probability Parameters

$\hat{x}_i$ symbol	$\hat{\beta}$	$\hat{\mu}$	$\hat{c}_a$	$\hat{\tau}_0$
$\hat{x}_i$ value	0.518	0.068	0.371	-0.020
σ_i	1.748	0.194	0.132	0.008
ϕ_i	1.717	0.147	0.131	0.008
e_{1j}	-0.0007	0.0453	0.1057	0.9934
e_{2j}	0.2411	-0.9049	0.3507	0.0041
e_{3j}	-0.1660	-0.3917	-0.8979	0.1133
e_{4j}	0.9562	0.1602	-0.2442	0.0194
Transients	$\hat{c}_s$	$\hat{c}_v$	$\hat{c}_e$	
parameters	0.442	1.050	1.076	

The values of σ_i in Table 1 are suitable for approximating P_4 near its maximum probability point. As described in Appendix A, an approximation over a broader range of parameters uses the values of σ_i to sample each principal component, computes the exact value of P_4 for each such sample, and then fits the result with normal distributions with scale parameters equal to the values of ϕ_i listed in Table 1.

2. Correlations

Results for 100 random samples using the values of ϕ_i listed in Table 1 are shown in Figures 1a, 1b, and 2. For these figures, values for μ and β have been used to find values for $c_{th} = 1/(\beta\mu)$ in order to make a more direct connection with the parameters appearing in the global heat balance equation 1.1. Also shown in these figures are large points for the maximum probability values listed in Table 1, along with linear regression fits between the ordinate and abscissa on each graph.

Values of climate sensitivity β have a positive correlation with the tropospheric aerosol efficacy c_a. Since the tropospheric aerosol forcing F_a is negative, increasing c_a decreases the radiative forcing, so a larger climate sensitivity is needed to maintain the observed temperature growth response τ' to the radiative forcing.

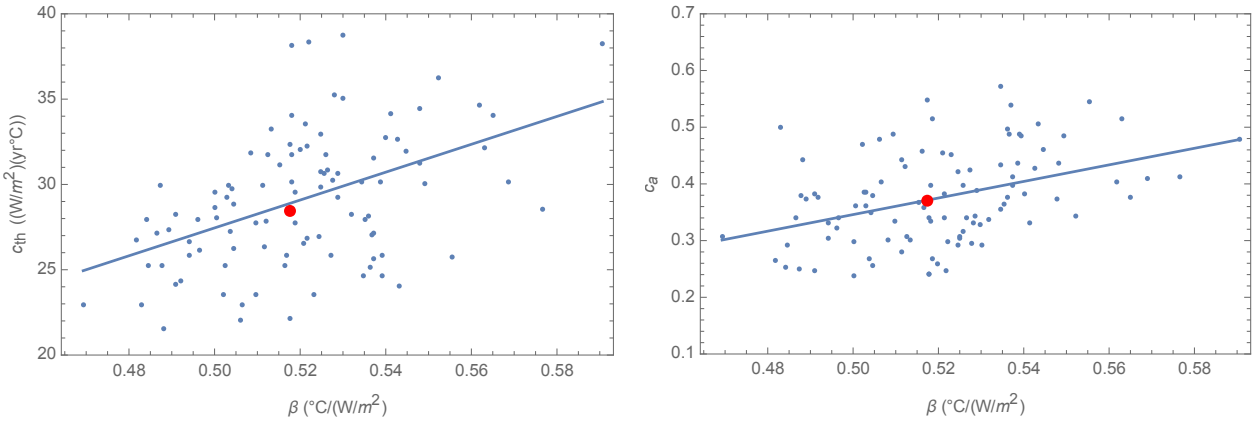

Figure 1. Random samples (small dots), maximum probability values (large dots) and linear regression line from the trivalent normal approximation for (a) $\{\beta, c_a\}$ and (b) $\{\beta, c_{th}\}$.

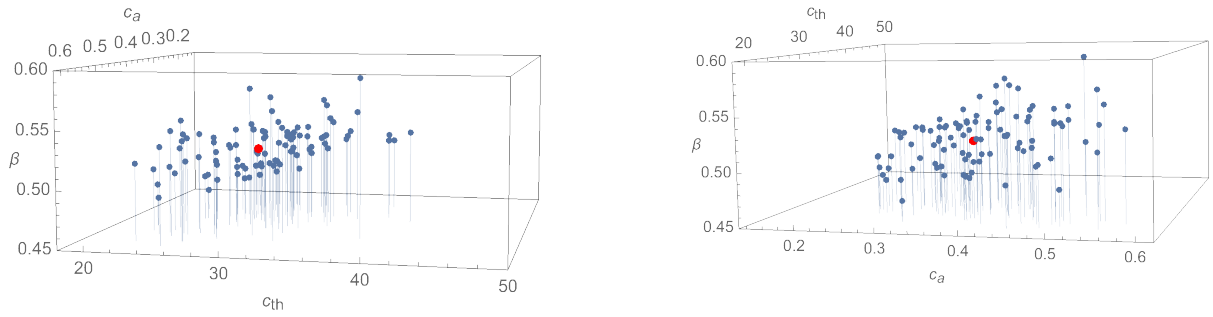

Figure 2. Two views of the same 100 random samples drawn of global heat balance equation parameters (small dots), and maximum probability values (large dots).

There is also a positive correlation of β with the thermal inertia parameter c_{th}. With the value $\hat{c}_a$ of tropospheric aerosol shielding listed in the first row of numbers in Table 1, and with increases in volcanic shielding over the preindustrial average removed as done here, total radiative forcing grew approximately exponentially after about 1906 (c.f. Figure 2a of CAGER4). If the radiative forcing is approximated as growing exponentially at a rate ν, then it can be shown that the temperature response is proportional to $1/(\nu c_{th} + \beta^{-1})$. In that case, larger values of β mean smaller values of β^{-1} and thus larger values of c_{th} to keep $1/(\nu c_{th} + \beta^{-1})$ constant. Then using transient corrected historical global average temperature data alone, there is no upper limit on β and c_{th} as long as $(\nu c_{th} + \beta^{-1})$ is kept constant. With this observation in mind, data on the global earth energy

imbalance was included here to limit the range of the upside tail in sampled values of c_{th} that is apparent in Figure 1a.

Figure 2 shows two views of triplets from the same samples used to produce Figures 1a and 1b. The view on the left in Figure 2 shows that the samples cluster around a plane, with a rise in the direction of increasing c_a. The view on the right in Figure 2 points out the increase in β with increasing c_{th} that is evident in Figure 1b.

3. Extrapolations of Global Average Temperature

This section presents two ways of looking at results of extrapolative solutions of the global heat balance equation (1.1).

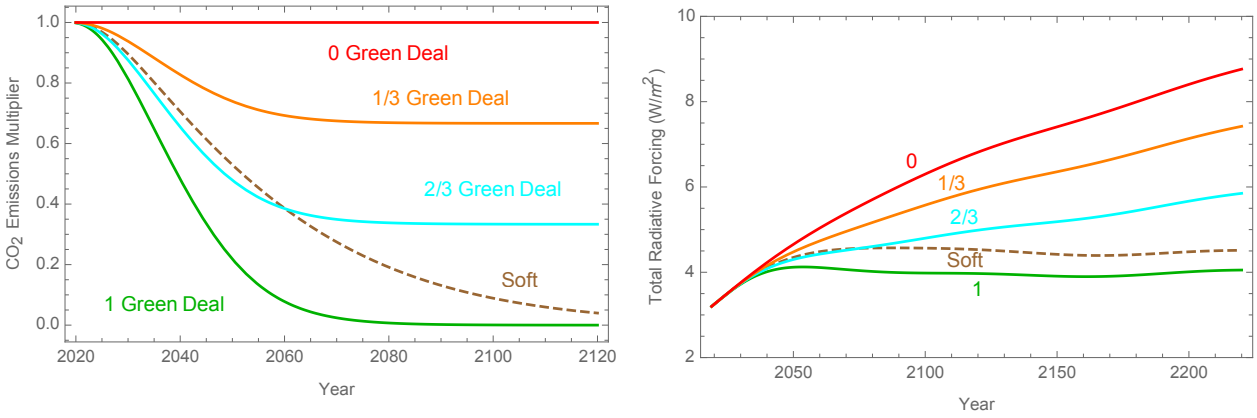

Figure 3. (a) Multipliers of extrapolated global anthropogenic atmospheric carbon emissions, and (b) corresponding evolutions of total radiative forcing.

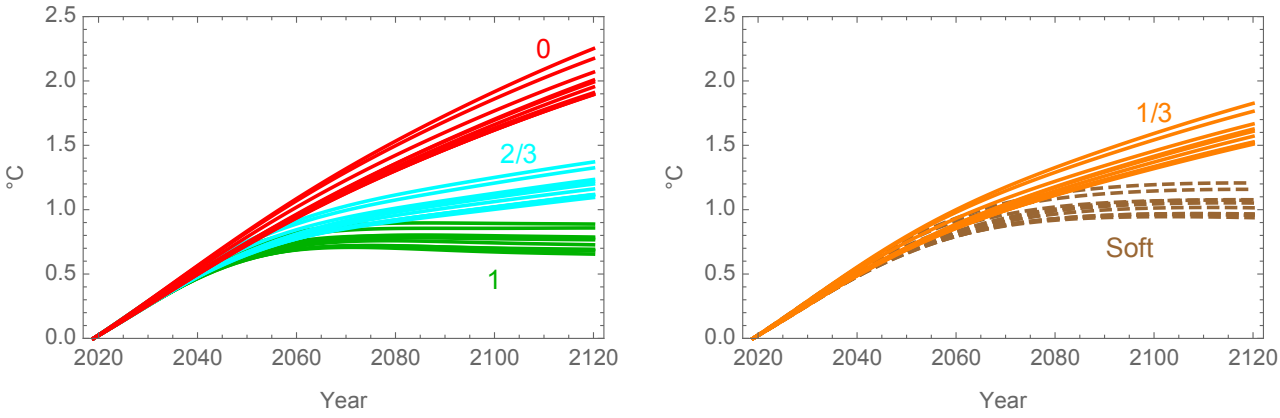

Figure 4. Increase of global average temperature from 2019 using ten random samples from trivalent normal approximation P_3 with (a) the 0, 2/3 and full Green Deal radiative forcing from Figure 3b, and (b) for the 1/3 Green Deal and Soft Green Deal cases shown in Figure 3b.

Figures 3a and 3b repeat extrapolations of global carbon emissions multipliers and total radiative forcing for five cases described in report CAGER5. Figures 4a and 4b show extrapolations of the increase in global average temperature for ten random samples of the heat balance equation parameters, for each of the five cases with total radiative forcing plotted in Figure 3b. The procedure for choosing random samples of the heat balance equation parameters is described in Appendix A. Figures 5a and 5b show cumulative probability distributions for the increases in global average

temperature over year 2019 for years 2100 and 2060 respectively. The large dots in Figures 5a and 5b bracket the 90% and 50% confidence regions and show the median results.

By 2060, the emissions limitations assumptions shown in Figure 3a have begun to separate the total radiative forcing amongst the different cases. However, the previous cumulative carbon emissions have left a legacy of atmospheric carbon accumulation that is only beginning to transport out of the atmosphere. By 2100, however, there are substantial differences in the outcomes for the results labelled 0, 1/3, 2/3, and 1 in Figure 5a.

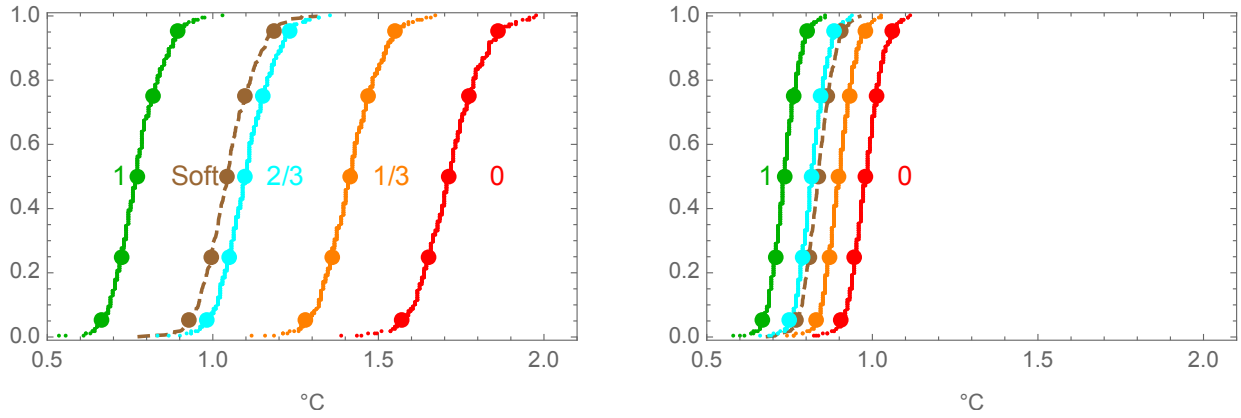

Figure 5. Cumulative probability distribution from the five radiative forcing evolutions in Figure 3b for global average temperature increase and (large dots) 90%, 50%, and 0% confidence regions (a) from 2019 to 2100, and (b) from 2019 to 2060.

Appendix A. Probability Distributions and Extrapolation Methods

A.1. **Probability Distribution Fits.** Following CAGER4, define

$$P_7 = \int_0^\infty d\sigma_\tau \int_0^\infty d\sigma_E \int_0^\infty d\sigma_{out} P/(\sigma_\tau \sigma_E \sigma_{out}) \tag{A.1}$$

Then define P_4 as the value of P_7 evaluated at the probability maximizing values $c_s = \hat{c}_s$, $c_v = \hat{c}_v$, and $c_e = \hat{c}_e$, with $P = P_\tau P_E$ where $P_\tau = (2\pi\sigma_\tau^2)^{-n_\tau/2} e^{-((1/2)\boldsymbol{\epsilon}_\tau \cdot \boldsymbol{\epsilon}_\tau/\sigma_\tau^2)}$ and

$$P_E = (2\pi\sigma_E^2)^{-n_E/2} e^{-((1/2)\boldsymbol{\epsilon}_E \cdot \boldsymbol{\epsilon}_E/\sigma_E^2)} (2\pi\sigma_{out}^2)^{-1/2} e^{-((1/2)\epsilon_{out}^2/\sigma_{out}^2)} \tag{A.2}$$

The denominator in the expression for P_4 is imposes an uninformative prior probability on the integration parameters [4]. Here $\boldsymbol{\epsilon}_\tau$ is a vector of $n_\tau = 74$ values of $\tau_G + \tau_H - \overline{\tau_G} + \tau_0 - \overline{\Delta\tau_{vs}} - \tau$. The vector $\boldsymbol{\epsilon}_E$ is a list of $n_E = 26$ values of $c_E E'_{th} - c_{th}\tau'$ with E'_{th} from annual differences of E_{th} for years 1990–2018, except for "outlier" value ϵ_{out} with E'_{th} computed from differences from the years 2002 and 2001 The transient-adjusted global average temperature data are $\tau_G = \tau_{GISTEMP} - c_s\tau_{solar} - c_v\tau_{volc} - c_e\tau_{ENSO}$, where $\tau_{GISTEMP}$ [5] is a list of temperature input data and τ_{solar}, τ_{volc}, and τ_{ENSO} are transient temperature changes as defined in CAGER3. Other parameters in $\boldsymbol{\epsilon}_\tau$ are $\tau_H = 0.82°\text{C}$, $\overline{\tau}_G = 0.421°\text{C}$, and $a_0 = \tau_0 - \overline{\Delta\tau_{vs}}$ with $\overline{\Delta\tau_{vs}} = -0.018°\text{C}$. The 74 values of τ used are

$$\tau_k = \left(F_k(1-\kappa)/\mu + \sum_{j=2}^{i-j} \kappa^2 e^{(k-j)\mu} F_j \right) / c_{th} \tag{A.3}$$

for years 1946–2019, with $\kappa = (1 - e^{-\mu})/\mu$ and $c_{th} - 1/(\beta\mu)$. The radiative forcing values of F_k for those years are the sums $F = F_{na} + c_a F_a$, where the tropospheric aerosol forcing F_a and the other contributions F_{na} contributions to radiative forcing are as described in CAGER1 and CAGER2. The vector $\boldsymbol{\epsilon}_{E*}$ is a list of $n_E = 26$ values of $c_E E'_{th} - c_{th}\tau'$ with E'_{th} computed from differences

in global stored energy for years 1991–2018 [8], with the exception of E'_{th} from the difference for 2001 and 2002 being used to compute ϵ_{out}. The constant $c_E = 0.62$ (W/m^2)yr/ZJ. Maximizing $\int_0^\infty d\sigma_\tau \int_0^\infty d\sigma_{E*} \int_0^\infty d\sigma_{out} P(\sigma_\tau \sigma_{E*} \sigma_{out})$ with respect to $\{\beta, \mu, c_a, \tau_0, c_s, c_v, c_e\}$ gives the values of those parameters listed in Table 1.

To obtain a first approximation to a functional fit to P_4, it is convenient to make linear transformations that rescale the variables to be non-dimensional and shift their zero values to the locations that maximize P_4. The new variables are $\beta_0 = (\beta - \hat{\beta})/\hat{\beta}$, $\mu_0 = (\mu - \hat{\mu})/\hat{\mu}$, $c_{a0} = (c_a - \hat{c}_a)/\hat{c}_a$, and $t_{00} = (\tau_0 - \hat{\tau}_0)/\hat{\tau}_0$. Using the identity [4],

$$\int_0^\infty x^{-(p+1)} e^{-ax^{-2}}\, dx = (1/2) a^{-(p/2)} \Gamma(p/2) \tag{A.4}$$

where $\Gamma(a) = \int_0^\infty t^{a-1} e^{-t} dt$, the function $\ln P_4$ is a constant plus

$$L_0 = (n_\tau/2) \ln(\boldsymbol{\epsilon}_\tau \cdot \boldsymbol{\epsilon}_\tau) + (n_E/2) \ln(\boldsymbol{\epsilon}_E \cdot \boldsymbol{\epsilon}_E) + (1/2) \ln(e^2_{out}) \tag{A.5}$$

with the substitutions $\beta = \hat{\beta}(1 + \beta_0)$, $\mu = \hat{\mu}(1 + \mu_0)$, $c_a = \hat{c}_a(1 + c_{a0})$, $\tau_0 = \hat{\tau}_{00}(1 + t_0)$ made in the above descriptions of $\boldsymbol{\epsilon}_\tau$, $\boldsymbol{\epsilon}_{E*}$ and ϵ_{out}. Letting $v_4 = \{\beta_0, \mu_0, c_{a0}, t_0\}$, the 4×4 (Hessian) matrix of the second derivatives of L_0 evaluated at $v_4 = \{0, 0, 0, 0\}$ has components $H_{ij} = d(dL_0/dv_i)/dv_j)|_{v_4 = \{0,0,0,0\}}$. The entries e_{ij} in Table 1 are the components of the eigenvectors of the inverse of H. The values of σ_i in Table 1 are the square roots of the eigenvalues of the inverse of H.
The function

$$P_{pc} = ((2\pi)^2 \sigma_1 \sigma_2 \sigma_3 \sigma_4)^{-1} e^{-(1/2)\sum_{i=1}^4 (v_i/\sigma_i)^2} \tag{A.6}$$

is an approximation to P_4 in the neighborhood of the maximum probability values of the arguments of P_4. The vectors v_i are known as principal components. Finding an approximation to P_4 over a wider range of its arguments starts with choosing 400 random samples of each of the components of v_i. Then the set of equations $v_i = \sum_{j=1}^4 e_{ij} x_j$ is inverted to give results for the x_i, and the exact expression for P_4 is computed for each set of 400 samples. A least squares fit to the same functional form as in equation A.4 results in the parameters ϕ_i instead of σ_i, as listed in the first row of numbers in Table 2.

A.1.1. *Integration over c_s, c_v, and c_e as Nuisance Parameters.* The results shown above used the probabilities evaluated at the probability maximizing values of c_s, c_v, and c_e listed in Table 1. A more computationally intensive approach is to integrate P_7 over c_s, c_v, and c_e treated as nuisance parameters. The ranges of c_s, c_v, and c_e covered during the numerical integration are $0.15 < c_s < 1.2$, $0.5 < c_v < 1.5$, and $0.5 < c_v < 1.5$. This region chosen to cover the region of appreciable probability while avoiding regions of space with extremely small probability. (An alternative is to integrate over c_s analytically and over the other two variables numerically, but this results in a very complicated expression for the analytic integral.) Parameters of quadrivalent normal fits to the result are shown in the second row of numbers in Table 2.

Table 2. Quadrivalent Normal Probability Parameters ϕ_i

Principal Component	1	2	3	4
Fixed Transient Parameters	1.717	0.147	0.131	0.0081
Integrated over Transient Parameters	1.782	0.150	0.145	0.0086

A.1.2. *Non-normal Distribution for v_2.* The scale parameters ϕ_i and σ_i in Table 1 are similar for each i, with the largest fractional difference being between ϕ_2 and σ_2. That observation suggested

examining an alternative to the normal distribution approximation for v_2. A slightly more accurate fit to the exact probability results as a replacement for $(2\pi)^{-1/2}e^{-(1/2)(v_2/\phi_2)^2}$ is

$$p_2 = h_2 e^{-((v_2-\xi_2)/\rho_2)^2)^{\kappa_2/2}} \tag{A.7}$$

with parameters listed in Table 3.

Table 3. Alternative with Kurtosis for p_2

Parameter	h_2	ξ_2	ρ_2	κ_2
Fixed Transient Parameters	2.795	-0.0097	0.2009	2.808
Integrated over Transient Parameters	2.732	-0.0059	0.2056	2.791

A.1.3. *Skew Normal Alternative for v_3.* A slightly more accurate fit to the exact probability results as a replacement for $(2\pi)^{-1/2}e^{-(1/2)(v_3/\phi_3)^2}$ is the skew normal function

$$p_3 = h_3 e^{-(1/2)(v_3-\xi_3)/\rho_3)^2}\mathrm{Erf}[1+\alpha_3(v_3-\xi_3)/\rho_3] \tag{A.8}$$

with parameters listed in Table 4.

Table 4. p_3 Skew Normal Function

Parameter	h_3	ξ_3	ρ_3	α_3
Fixed Transient Parameters	2.480	-0.0081	0.1608	0.7141
Integrated over Transient Parameters	2.441	-0.0770	0.1634	0.5056

A.2. **Comparing Extrapolations with Different Probability Function Approximations.** Table 5 compares points on cumulative probability distributions for temperature increase from 2019 to 2100 as in Figure 5a, using sampling from four different approximations to the probability function P_4 for fixed values of the transient correction multipliers and four approximations for integration of P_7 over those parameters.

Table 5. 2019–2100 °C Change Confidence Limits

Confidence Level	5%	25%	50%	75%	95%
Fixed Transient Parameters					
Quadrivalent Normal	1.58	1.66	1.72	1.78	1.87
With p_2 Alternative	1.56	1.66	1.71	1.77	1.87
With p_3 Alternative	1.53	1.64	1.72	1.79	1.89
With p_2 and p_3 Alternatives	1.53	1.64	1.71	1.79	1.87
Integrated over Transient Parameters					
Quadrivalent Normal	1.53	1.64	1.72	1.78	1.88
With p_2 Alternative	1.54	1.64	1.71	1.78	1.89
With p_3 Alternative	1.57	1.67	1.72	1.77	1.83
With p_2 and p_3 Alternatives	1.59	1.67	1.72	1.76	1.82

Users of these results can choose whichever approximation to the probability distribution that suits their needs. For subsequent CAGE reports, the simplest to calibrate and sample is the quadrivalent normal approximation with fixed transient parameters, which leads to the first row of numbers in Table 6. The approximation that is most elaborate but is more complicated to calibrate and sample gives the last row of numbers in Table 6. For subsequent work for CAGE where probability distribution sampling may be required, the use of the simpler quadrivalent normal approximation with fixed transient parameters is planned.

A.2.1. *Trivalent Normal vs. Quadrivalent Normal Approximation Results.* That the value of the scale parameter listed in Table 2 for fourth principal component is so much smaller than the other three is an indication that a reasonably accurate trivalent normal approximation to the probability distribution can be found. That is done by setting $v_4 = 0$ to find coefficients $\{r_1, r_2, r_3\} = -\{e_{41}, e_{42}, e_{43}\}/e_{44}$ of the approximation $x_4 = r_1 x_1 + r_2 x_2 + r_3 x_3$. Using this result to eliminate x_4 from the set of equations $v_i = \sum_{j=1}^{4} e_{ij} x_j$ for $i = 1 \dots 4$ gives a result of the form $w_i = \sum_{j=1}^{3} M_{ij} x_j$ for $i = 1 \dots 3$. A trivalent normal function of the w_i does provide a reasonably good approximation. However, the slight reduction in the number of samples needed would come at the cost of some loss in accuracy and a more complicated procedure for updating the calibration against observational data.

A.3. **Sampling.** Values of random samples of the components of v_i are $\sqrt{2\sigma_i}\,\text{ErfInverse}(2R-1)$, where R is a random number between 0 and 1 and ErfInverse(z) is solution for x of $z = \text{Erf}(x)$. For each of the resulting components of v_4, finding the corresponding values of $\{\beta, \mu, c_a, \tau_0\}$ and using those to compute the corresponding values of P_{4i} for $i = 1 \dots 4$ is straightforward.

The cumulative integral of p_2 to be used for finding random samples is

$$\int_{-\infty}^{x} p_2\, dx = (s + 1 - sQ_2)/2 \tag{A.9}$$

with $Q_2 = Q(\kappa_2^{-1}, (x - \xi_2)s/\rho)$, and $s = \text{Sign}(x - \xi_2)$. The function Sign as used here takes on the value -1 for negative arguments and the value +1 for non-negative arguments. The regularized incomplete gamma function is $Q(a, z) = \Gamma(a, z)/\Gamma(a, 0)$. The incomplete gamma function is $\Gamma(a, z) = \int_z^\infty t^{a-1} e^{-t} dt$. Random samples of v_2 are given by

$$\xi_2 + s_R \rho\, \text{InverseRegularizedGamma}(\kappa_2^{-1}, 1 - (2R-1)s_R) \tag{A.10}$$

where $s_R = \text{Sign}(2R-1)$ and R is a random number between 0 and 1. The solution for z of the equation $r = Q(a, z)$ is the function InverseRegularizedGamma(a, r).

The skew normal function also has analytic cumulative probability function that can be expressed as a sum of special functions available in some software packages. Inverting and sampling the resulting expression appears also to be more trouble than it is worth to avoid using numerical integration procedures. That is because the required integrals described here can also be computed numerically and the sampling equations solved numerically as done for Figure 4b, but various software platforms have built-in procedures or functions that avoid a need for numerical integrations or solution searches. A similar procedure can be used if available software has a built-in function inverse skew normal calculator.

However, a simple and sufficiently efficient procedure used herein for sampling non-normal distribution function approximations is to interpolate the cumulative distributions computed numerically and solve for the values of the argument of the cumulative distribution that gives results equal to a set of random numbers each between 0 and 1.

A.4. **Temperature Extrapolation Methods.** The global heat balance equation is integrated numerically, from an initial condition as a continuous function of time. The differential equation solved is $c_{th} d\tau/dt = F_{na} + c_a F_a - \tau/\beta$. The initial conditions are the analytic solutions integrated from $\tau = 0$ in 1750. The resulting value of τ for 2019 is computed using the values of $\{\beta, \mu, c_a\}$ for each sample.

References

[1] Singer, C. and L. Matchett, 2015. Climate action gaming experiment: Methods and example results, *Challenges* **6**, 202–228, doi:10.3390/challe6020202.

[2] Ding, C., and C. Singer. 2022. University of Illinois at Urbana-Champaign Program in Arms Control & Domestic and International Security Research Reports ACDIS//ACDIS DIN:1, Climate Action Game Experiment motivation and role of radiative forcing; DIN:2, Calibration and extrapolation of a simple global carbon balance model; DIN:3, Non-anthropogenic influences on global average temperature; DIN:4, Global heat balance model parameters; DIN:5, Extrapolations of global average temperature, sea level rise, and ocean pH change; https://acdis.illinois.edu/outreach/research/research-reports.

[3] IPCC, 2021. *Climate Change 2021: The Physical Science Basis. Contribution of Working Group I to the Sixth Assessment Report of the Intergovernmental Panel on Climate Change*, V. Masson-Delmotte, P. Zhai, A. Pirani, S. L. Connors, C. Pèan, S. Berger, N. Caud, Y. Chen, L. Goldfarb, M. I. Gomis, M. Huang, K. Leitzell, E. Lonnoy, J. B. R. Matthews, T. K. Maycock, T. Waterfield, O. Yelekçi, R. Yu and B. Zhou (eds.). Cambridge University Press. In Press, https://www.ipcc.ch/report/sixth-assessment-report-working-group-i/.

[4] Box, G. E. P., and G. C. Tiao. 1992. *Bayesian Inference in Statistical Analysis*, New York: Wiley.

[5] GISTEMP Team. 2021. *GISS Surface Temperature Analysis (GISTEMP), version 4.* NASA Goddard Institute for Space Studies, https://data.giss.nasa.gov/gistemp/; https://data.giss.nasa.gov/gistemp/tabledata_v4/GLB.Ts+dSST.csv, accessed December 22, 2021.

[6] Foster, G., and S. Rahmstorf. 2011. Global temperature evolution 1979–2020, *Environmental Research Letters* **6**, 044022, http://dx.doi.org/10.1088/1748-9326/6/4/044022.

[7] Hawkins, E., P. Ortega, E. Suckling, A. Schurer, G. Heferl, P. Jones, M. Joshi, T. J. Osborn, V. Masson-Delmotte, J. Mignot, P. Thorne, and G. J. van Oldenborgh. 2017. Estimating changes in global temperature since the preindustrial period, *Bulletin of the American Meteorological Society*, September, 1841–1856, https://doi.org/10.1175/BAMS-D-16-0007.1.

[8] von Schuckmann, K., L.Cheng, M. D. Palmer, J. Hansen, C. Tassone, V. Aich, S. Adusumilli, H. Beltrami, T. Boyer, F. J. Cuesta-Valero, D. Desbruyères, C. Domingues, A. García-García, P. Gentine, J. Gilson, M. Gorfer, L. Haimberger, M. Ishii, G. C. Johnson, R. Killick, B. A. King, G. Kirchengast, N. Kolodziejczyk, J. Lyman, B. Marzeion, M. Mayer, M. Monier, D. P. Monselesan, S. Purkey, D. Roemmich, A. Schweiger, S. L. Seneviratne, A. Shepherd, D. A. Slater, A. K. Steiner, F. Straneo, M.-L. Timmermans, and S. E. Wijffels. 2020. Heat stored in the Earth system: where does the energy go? *Earth System Science Data* **12**, 2013–2041, https://doi.org/10.5194/essd-12-2013-2020.